with Earth's Theia component; thus, it is presently not possible to obtain information on $\Delta^{17}O$ of the proto-Earth.

An alternative explanation for the isotope difference between Earth and the Moon is that the $\Delta^{17}O$ value of Earth was modified by late-accreting material (late veneer) after the formation of the Moon. Such material may have had a $\Delta^{17}O$ value lower than that of Earth. In the following scenario, Earth and the Moon had identical $\Delta^{17}O$ compositions after the giant impact (*4*, *8*, *15*–*17*), with the Moon now representing the composition of Earth before the late veneer.

From the overabundance of siderophile elements in Earth's mantle, late veneer masses between 0.1 and 0.5% of BSE have been suggested (*28*). Higher estimates between 0.3 to 0.8% of BSE are derived from ^{182}W isotope systematics (*29*). Here, we use 0.5% for mass balance considerations. The only groups of undifferentiated meteorites that have $\Delta^{17}O$ much lower than that of Earth are carbonaceous chondrites (*30*). Assuming that the late veneer component had an oxygen isotope composition of CV carbonaceous chondrites ($\Delta^{17}O$ = –4‰) (*30*), incorporation of 0.5% late veneer component would decrease the $\Delta^{17}O$ of Earth by as much as ~20 ppm. Similar proportions of material resembling CO, CR, or CH carbonaceous chondrites would also be sufficient to explain the observed difference of 12 ppm between Earth and the Moon.

If this scenario is correct, the observed difference in $\Delta^{17}O$ between Earth and the Moon points toward a late veneer that is dominated by carbonaceous chondrites. Among the carbonaceous chondrites, the most water-rich meteorites are found. It would thus be feasible that part of the ocean water was delivered by the late veneer impactors. Evidence for this scenario may be found in old crust that has escaped mixing with the late veneer component (*29*).

REFERENCES AND NOTES

1. S. R. Taylor, in *Encyclopedia of the Solar System*, L.-A. McFadden, P. R. Weissman, T. V Johnson, Eds. (Academic Press, San Diego, ed. 2, 2007), pp. 227–250.
2. A. G. W. Cameron, W. Benz, *Icarus* **92**, 204–216 (1991).
3. R. M. Canup, E. Asphaug, *Nature* **412**, 708–712 (2001).
4. K. Pahlevan, D. J. Stevenson, *Earth Planet. Sci. Lett.* **262**, 438–449 (2007).
5. R. N. Clayton, L. Grossman, T. K. Mayeda, *Science* **182**, 485–488 (1973).
6. R. N. Clayton, T. K. Mayeda, *Proc. Lunar Sci. Conf.* **6**, 1761–1769 (1975).
7. R. N. Clayton, T. K. Mayeda, *Geochim. Cosmochim. Acta* **60**, 1999–2017 (1996).
8. U. Wiechert *et al.*, *Science* **294**, 345–348 (2001).
9. M. Spicuzza, J. Day, L. Taylor, J. Valley, *Earth Planet. Sci. Lett.* **253**, 254–265 (2007).
10. L. J. Hallis *et al.*, *Geochim. Cosmochim. Acta* **74**, 6885–6899 (2010).
11. J. Zhang, N. Dauphas, A. Davis, I. Leya, A. Fedkin, *Nat. Geosci.* **5**, 251–255 (2012).
12. J. I. Simon, D. J. De Paolo, *Earth Planet. Sci. Lett.* **289**, 457–466 (2010).
13. C. Fitoussi, B. Bourdon, *Science* **335**, 1477–1480 (2012).
14. M. Touboul, T. Kleine, B. Bourdon, H. Palme, R. Wieler, *Nature* **450**, 1206–1209 (2007).
15. R. M. Canup, *Science* **338**, 1052–1055 (2012).
16. M. Ćuk, S. T. Stewart, *Science* **338**, 1047–1052 (2012).
17. A. Reufer, M. M. M. Meier, W. Benz, R. Wieler, *Icarus* **221**, 296–299 (2012).
18. C. Münker *et al.*, *Science* **301**, 84–87 (2003).
19. A. Pack, D. Herwartz, *Earth Planet. Sci. Lett.* **390**, 138–145 (2014).
20. See supplementary materials on *Science* Online.
21. E. Young, A. Galy, H. Nagahara, *Geochim. Cosmochim. Acta* **66**, 1095–1104 (2002).
22. P. H. Warren, *Earth Planet. Sci. Lett.* **311**, 93–100 (2011).
23. R. N. Clayton, T. K. Mayeda, A. E. Rubin, *J. Geophys. Res.* **89**, C245–C249 (1984).
24. J. Newton, I. A. Franchi, C. T. Pillinger, *Meteorit. Planet. Sci.* **35**, 689–698 (2000).
25. M. Javoy *et al.*, *Earth Planet. Sci. Lett.* **293**, 259–268 (2010).
26. A. Trinquier, J. Birck, C. Allègre, *Astrophys. J.* **655**, 1179–1185 (2007).
27. M. Regelous, T. Elliott, C. D. Coath, *Earth Planet. Sci. Lett.* **272**, 330–338 (2008).
28. R. J. Walker, *Chem. Erde* **69**, 101–125 (2009).
29. M. Willbold, T. Elliott, S. Moorbath, *Nature* **477**, 195–198 (2011).
30. R. N. Clayton, T. K. Mayeda, *Geochim. Cosmochim. Acta* **63**, 2089–2104 (1999).
31. A. Bischoff, M. Horstmann, A. Pack, M. Laubenstein, S. Haberer, *Meteorit. Planet. Sci.* **45**, 1638–1656 (2010).

ACKNOWLEDGMENTS

We thank NASA for providing samples; Z. Sharp, F. Wombacher, C. Münker, and H. Palme for discussions; three anonymous reviewers for constructive comments; and E. Barkan and B. Luz for analyzing our reference O_2 relative to SMOW. All data are provided within the manuscript or the supplementary materials.

SUPPLEMENTARY MATERIALS

www.sciencemag.org/content/344/6188/1146/suppl/DC1
Materials and Methods
Supplementary Text
Figs. S1 to S6
Table S1
References (*32*–*41*)

21 January 2014; accepted 8 May 2014
10.1126/science.1251117

PLANETARY FORMATION

Protracted core formation and rapid accretion of protoplanets

T. S. Kruijer,[1,2] M. Touboul,[3] M. Fischer-Gödde,[1] K. R. Bermingham,[3] R. J. Walker,[3] T. Kleine[1]

Understanding core formation in meteorite parent bodies is critical for constraining the fundamental processes of protoplanet accretion and differentiation within the solar protoplanetary disk. We report variations of 5 to 20 parts per million in ^{182}W, resulting from the decay of now-extinct ^{182}Hf, among five magmatic iron meteorite groups. These ^{182}W variations indicate that core formation occurred over an interval of ~1 million years and may have involved an early segregation of Fe-FeS and a later segregation of Fe melts. Despite this protracted interval of core formation, the iron meteorite parent bodies probably accreted concurrently ~0.1 to 0.3 million years after the formation of Ca-Al–rich inclusions. Variations in volatile contents among these bodies, therefore, did not result from accretion at different times from an incompletely condensed solar nebula but must reflect local processes within the nebula.

Magmatic iron meteorites are generally considered to sample the metal cores of differentiated protoplanetary bodies that formed after the segregation and subsequent crystallization of metallic melts (*1*). Each of the magmatic iron meteorite groups represents metal from a distinct parent body. The groups are primarily distinguished by different contents of moderately volatile elements such as Ga and Ge, relative to Ni. The order-of-magnitude variations in volatile depletion probably arise from chemical fractionations induced by processes within the solar nebula, suggesting that the conditions of parent body accretion varied in time and/or space.

Precise determination of the timing of core formation for each magmatic iron meteorite group is critical for determining the accretion rate for each parent body, for identifying the heat sources responsible for melting and differentiation, and for assessing whether the timing of accretion played a role in establishing the different degrees of volatile depletion observed in the magmatic iron meteorite groups. The extinct ^{182}Hf-^{182}W chronometer [half-life ($t_{1/2}$) = 8.9 million years (My)] is ideally suited to precisely constrain the time of core formation, but its application to iron meteorites has been hampered by cosmic ray–induced neutron capture effects on W isotope compositions (*2*–*5*). Thus, although previous studies have shown that core formation in most iron meteorite parent bodies probably occurred within ~2 My after the formation of Ca-Al–rich inclusions (CAIs), it has not yet been possible to resolve differences in the timing of accretion and core formation (*6*).

We used Pt isotope compositions to quantify and correct measured W isotope compositions of iron meteorites for the effects of neutron capture (*7*, *8*) and obtained combined high-precision Pt

[1]Institut für Planetologie, Westfälische Wilhelms-Universität Münster, Wilhelm-Klemm-Strasse 10, DE-48149 Münster, Germany. [2]ETH Zürich, Inst. of Geochemistry and Petrology, Clausiusstrasse 25, CH-8092 Zürich, Switzerland. [3]Department of Geology, University of Maryland, College Park, MD 20742, USA.

and W isotope data for metal samples from the major iron meteorite groups (IIAB, IID, IIIAB, IVA, and IVB) (*9*). All iron meteorite groups exhibit well-defined empirical ε^{182}W-ε^{196}Pt correlations, whose intercepts provide pre-exposure ε^{182}W (the ^{182}W/^{184}W unbiased by galactic cosmic rays) for each group (Fig. 1 and table S1). Our results reveal small but resolvable differences in pre-exposure ε^{182}W among magmatic iron meteorite groups, with the IID iron meteorites having the highest pre-exposure ε^{182}W of −3.15 ± 0.07 (±95% confidence) and the IIAB iron meteorites having the lowest value of −3.40 ± 0.03. Model ages of metal segregation in the iron meteorite parent bodies, relative to the formation of CAIs, can be calculated as the time of Hf/W fractionation from an unfractionated reservoir with chondritic ^{180}Hf/^{184}W of 1.28 ± 0.03 (*10*, *11*). At face value, the distinct pre-exposure ε^{182}W values yield resolved and very precise Hf-W ages spanning a total range of ~0.7 to ~2.9 My after CAI formation (table S6).

With the exception of the IID iron meteorites, the pre-exposure ε^{182}W values exhibit inverse correlations with Ga/Ni and S contents, estimated for the bulk compositions of each core (Fig. 2). This suggests that the degree of volatile element depletion exerted some control on the timing of core formation. The inverse correlation of core formation model age with the degree of volatile depletion is remarkable because it is opposite to what might be expected for the accretion time of iron meteorite parent bodies. Volatile-poor bodies (such as IVA and IVB) would be expected to have accreted earlier, at a time when the solar nebula was yet not fully condensed, in comparison to more volatile-rich bodies (such as IIAB) (*12*, *13*). Our data, however, suggest that core formation in the IVA and IVB iron meteorite parent bodies occurred later than in the IIAB parent body (Fig. 2 and table S1). This may indicate that the IVA and IVB, as well as the IID, parent bodies accreted later than or over a longer period of time than the IIAB parent body. However, linking the time of core formation to an age of accretion requires knowledge of the temperature at which melting and metal segregation occurred. This temperature is largely controlled by the S content of the iron meteorite parent bodies (*14*, *15*), and thus was different for each body. The IIAB iron meteorites have the highest S content and hence the lowest liquidus temperature of ~1330°C, whereas the IVB iron meteorites exhibit the lowest S content and highest liquidus temperature of ~1600°C. The inverse ε^{182}W-versus-S correlation observed among the magmatic iron meteorites therefore may primarily reflect different melting temperatures of the metal within their parent bodies.

To quantify the relation between accretion age and time of melting and metal segregation, we consider two end-member models for core formation (*9*). After the initial accretion, the still undifferentiated iron meteorite parent bodies probably consisted of an unequilibrated mix of different components, including metallic Fe, FeS, and silicates. Upon heating, due primarily to the presence of ^{26}Al, melting probably began at the Fe-FeS eutectic temperature (~1000°C at 1 atm) (*14*) (Fig. 3). The first model assumes that this Fe-FeS melt did not segregate, but that heating continued to the liquidus temperature of the core, and only then did the metal melt segregate to form the core. In this model, the observed ~1-My time difference in core formation model ages between the IIAB and IVA parent bodies is consistent with the time required to raise the temperature inside the parent body from the liquidus temperature of the IIAB to that inferred for the IVA iron meteorites (Fig. 3). Despite their different core formation ages, the IIAB, IIIAB, and IVA iron meteorite parent bodies, therefore, could have accreted within a narrow time

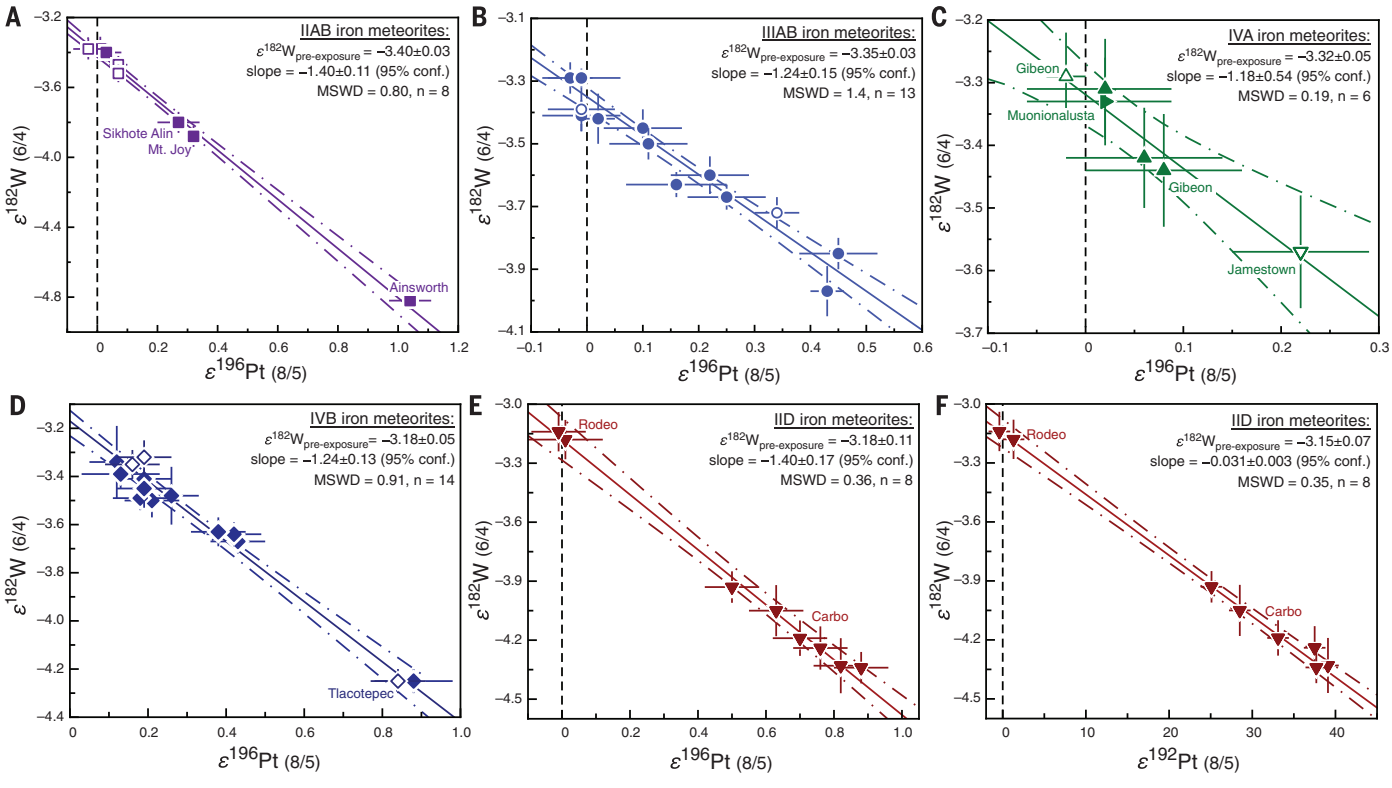

Fig. 1. ε^{182}W versus ε^{i}Pt for the major magmatic iron meteorite groups. (**A** to **F**) IIAB, IIIAB, IVA, IVB, and IID iron meteorites, respectively. ε^{182}W (6/4) and ε^{19i}Pt (8/5) are 0.01% deviations from the terrestrial ^{182}W/^{184}W ratios (normalized to ^{186}W/^{184}W, denoted 6/4) and ^{i}Pt/^{195}Pt ratios (normalized to ^{198}Pt/^{195}Pt, denoted 8/5). Solid lines are best-fit regressions through the data with their 95% confidence envelopes (dashed lines) and pre-exposure ε^{182}W intersecting the ordinate at ε^{i}Pt = 0. W isotope analyses were performed using multicollector inductively coupled plasma mass spectrometry (solid symbols) or thermal ionization mass spectrometry (open symbols). Error bars represent external uncertainties (2 SD for Pt and 95% confidence for W). The investigated IID iron meteorites Carbo and Rodeo have nearly identical Ir/Pt, so in this specific case, ε^{182}W (6/4) versus ε^{192}Pt (8/5) also show a well-defined correlation (Fig. 1F), providing an additional precise estimate of the pre-exposure ε^{182}W (*7*). Small downward corrections for nucleosynthetic heterogeneity have been made to the IID and IVB data points (*7*, *9*).

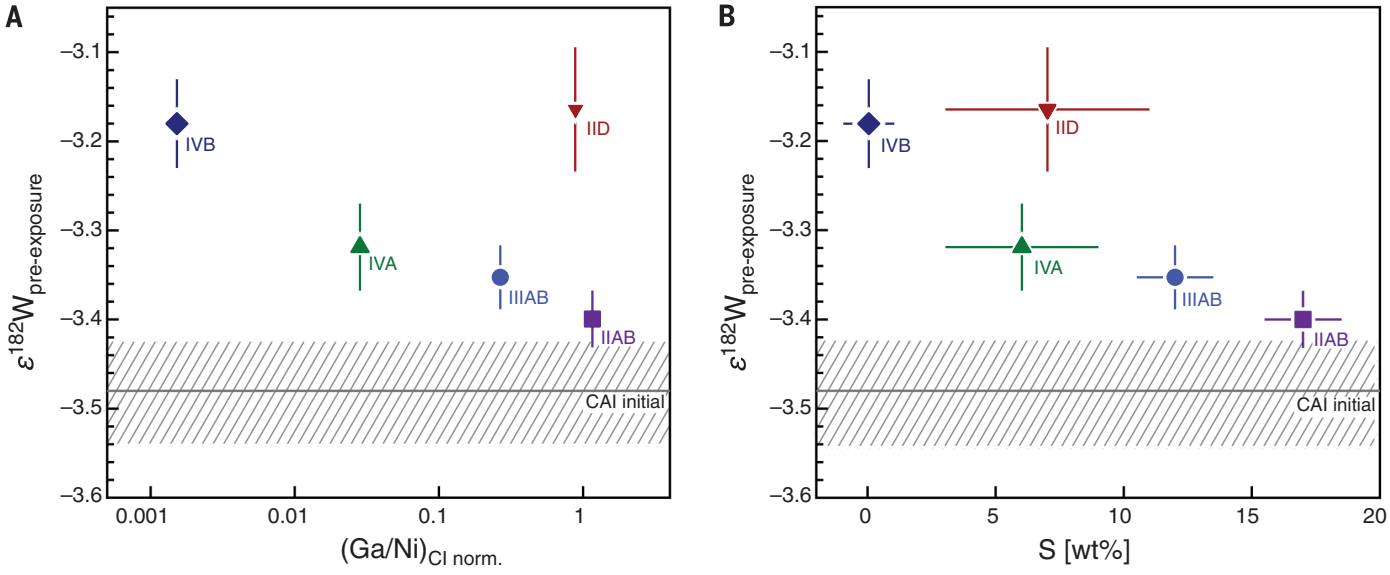

Fig. 2. ε^{182}W versus volatile element ratios and bulk S contents. (**A**) Pre-exposure ε^{182}W versus CI chondrite–normalized Ga/Ni. (**B**) Pre-exposure ε^{182}W versus inferred S concentration (weight %) in the core (*9*). Error bars on ε^{182}W represent 95% confidence limits of the mean. The Ge, Ga, and Ni concentrations are from (*19*) and references therein.

interval, between ~0.1 and ~0.3 My after the formation of CAIs. However, for a given accretion time, this model cannot explain the higher ε^{182}W of the IID and IVB iron meteorites, which plot to the right of the heating curves of the IIAB, IIIAB, and IVA groups (Fig. 3).

The second model assumes that, as a consequence of their high densities, the Fe-FeS eutectic melts rapidly segregated by permeable flow to form cores (*16*). The parent bodies subsequently continued to heat, eventually leading to the melting of silicates and finally of pure Fe metal at ~1600°C (*14*). Therefore, in this model, core formation and metal-silicate separation began with eutectic melting of Fe-FeS but probably did not resume until pure Fe metal melted at higher temperatures (Fig. 3). Because melting was a multistage process occurring over a period of time, the early-segregated Fe-FeS melts would have had less radiogenic ε^{182}W than the later-segregated pure Fe metal melts. In addition, as the early-segregated Fe-FeS melts removed some W to the initial cores, the residual mantles would have developed suprachrondritic $^{180}Hf/^{184}W$, potentially leading to considerably higher ε^{182}W in the mantles over a short period of time. The final W isotope compositions of the metal cores therefore would reflect particular mixes of early- (having lower ε^{182}W) and late- (having higher ε^{182}W) segregated metal fractions. Consequently, for different bodies with uniform formation ages, the metal cores of S-rich bodies would be characterized by lower ε^{182}W as compared to S-poor bodies, because they would contain a larger fraction of the early-segregated Fe-FeS melt.

We modeled the ^{182}W evolution in the iron meteorite parent bodies, accounting for the $^{180}Hf/^{184}W$ in the mantles after a first melt extraction (Fig. 4A). For an accretion time of 0.25 My, our thermal model predicts that the first Fe-FeS melts formed at ~0.7 My (t_1 in Fig. 4) and that the melting temperature of pure Fe metal was reached ~0.6 My later, at ~1.3 My (t_2 in Fig. 4). For an earlier accretion time, at ~0.1 My, the difference between t_1 and t_2 becomes much smaller, leaving too little time for the generation of a significant ^{182}W difference between early- and late-segregated metal. For accretion times later than ~0.3 My, the onset of melting is too late to explain the low ε^{182}W of –3.40 ± 0.03 of the IIAB iron meteorites. The $^{180}Hf/^{184}W$ of the mantle after extraction of an Fe-FeS melt at t_1 is obtained by estimating the fraction of Fe metal melted at the eutectic, using the S content of each iron meteorite group (*9*). The $^{180}Hf/^{184}W$ values of the mantles reached after a first melt extraction are different for each parent body, because the amount of early-segregated Fe-FeS melt decreases with decreasing S content of the bulk core. Thus, the mantles of S-rich bodies (such as IIAB and IID) initially have higher $^{180}Hf/^{184}W$ than those of S-poor bodies (such as IVA) (Fig. 4A). After extraction of a Fe-FeS melt, the mantles of the iron meteorite parent bodies evolved to ε^{182}W values between ~ –3.3 and –3.1 until the melting temperature of pure Fe metal was reached (Fig. 4A). At that point, all Fe metal segregated to the core and was mixed with the earlier-segregated Fe-FeS melts. The IIAB iron meteorites have a very low ε^{182}W of –3.40 ± 0.03 that is only slightly elevated as compared to the

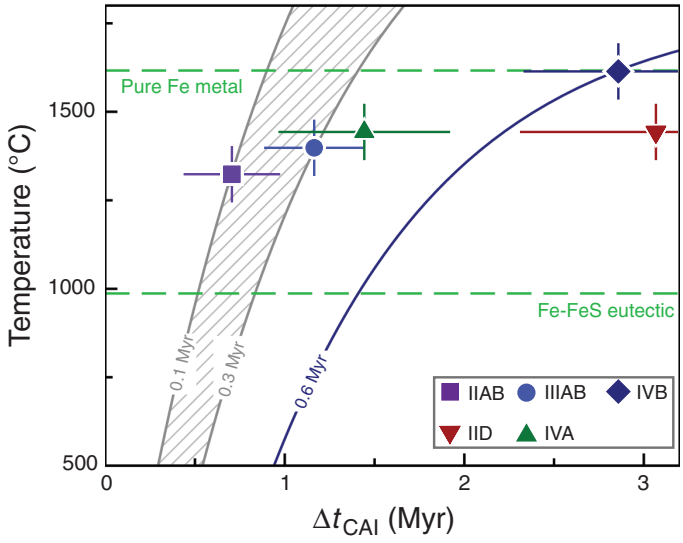

Fig. 3. Internal temperature versus time after CAI formation for iron meteorite parent bodies assuming a single event of metal segregation. Solid symbols show the model ages of metal segregation inferred for the iron meteorite parent bodies. Also shown are model results for postaccretional internal heating by ^{26}Al decay of a spherical protoplanet with a radius of 40 km (*9*). Solid curves show the temperature evolution at half the radius (i.e., at 20 km depth) in planetesimals accreted at 0.1 to 0.3 My (hashed area) after CAI formation, and for 0.6 My in the case of the IVB iron meteorites (dark blue curve). Horizontal dashed lines show the eutectic melting temperature in the Fe-FeS system and that of pure Fe at atmospheric pressure.

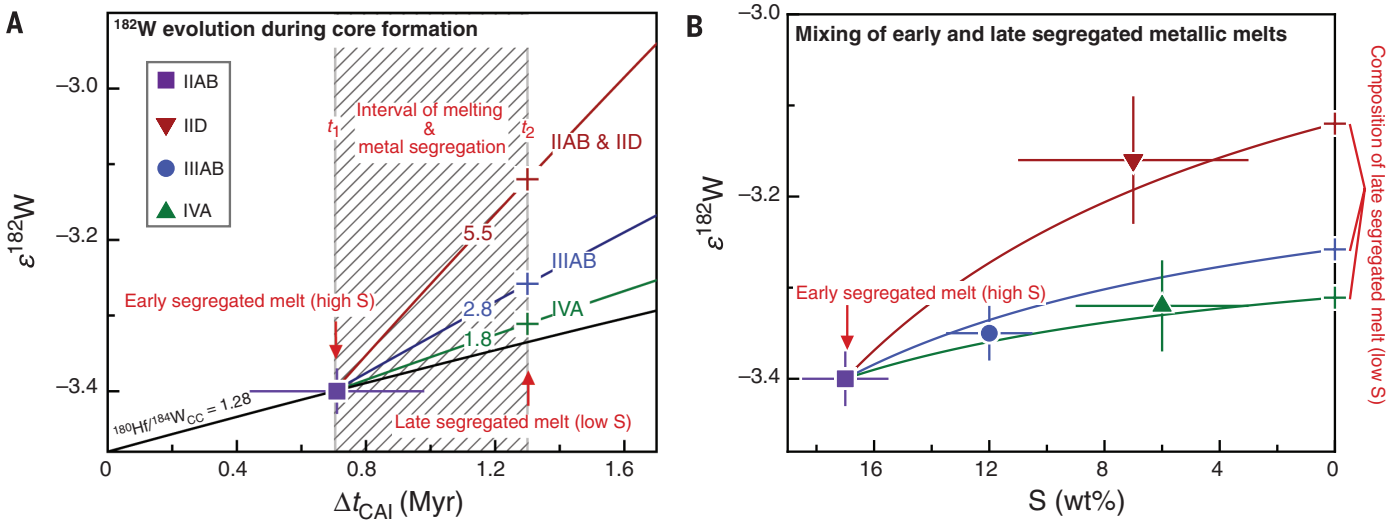

Fig. 4. History of core formation for a two-stage metal segregation process. (**A**) ε^{182}W evolution diagram illustrating the effect of a two-step metal segregation history of the IIAB, IIIAB, IVA, and IID parent bodies, shown for an accretion time of 0.25 My after CAI formation. For a given accretion time, the thermal model constrains the time interval (hashed area) of melting and core formation between the early (t_1) and late (t_2) metal segregation step. Dashed lines show modeled ε^{182}W curves for different ^{180}Hf/^{184}W ratios of the IID, IIIAB, and IVA residual mantles after early core segregation at t_1, represented by the IIAB iron meteorites. The modeled ε^{182}W compositions of the late-segregated (low-S) core fractions at t_2 are also plotted. (**B**) Diagram of ε^{182}W versus S for the IIAB, IID, IIIAB, and IVA iron meteorite groups with mixing curves demonstrating that the pre-exposure ε^{182}W of the IID, IIIAB, and IVA iron meteorites can be explained by mixing of (i) an early- (high-S) segregated melt, represented by the IIAB iron meteorites, and (ii) the modeled ε^{182}W compositions of the residual mantles, which supplied a late- (low-S) segregated melt.

solar system initial value of −3.48 ± 0.06, indicating that melting and metal segregation in the IIAB iron meteorite parent body must have started very early. The IIAB composition, therefore, is dominated by the early-segregated Fe-FeS melt and as such represents one end member in the mixing model. The mixing of early- and late-segregated metal to form bulk iron cores illustrates that the variable ε^{182}W, as well as the inverse ε^{182}W–versus-S correlation of the magmatic iron meteorites, can be reproduced (Fig. 4B). The mixing model also reproduces the offset of the IID iron meteorites from the ε^{182}W–versus-S correlation, which reflects the high ^{180}Hf/^{184}W of the IID mantle after extraction of an early Fe-FeS melt.

Only the IVB iron meteorites appear inconsistent with the models presented above. They are strongly depleted in volatile elements, including S (*17*, *18*). Therefore, only a very minor early-segregated Fe-FeS metal fraction could form, and so this body evolved with chondritic ^{180}Hf/^{184}W until pure Fe melted at high temperature and subsequently segregated to form the core. However, for accretion times of ~0.1 to 0.3 My, our model predicts that the melting temperature of pure Fe is reached between ~0.7 and 1.3 My after CAI formation (Fig. 3); that is, earlier than suggested by the Hf-W model age of 2.9 ± 0.5 My for the IVB iron meteorites. Thus, either the IVB parent body accreted later than the other iron meteorite parent bodies (at ~0.6 My after CAI formation; Fig. 3), or the precursor material of the IVB parent body had higher-than-chondritic Hf/W. The inferred bulk composition of the IVB parental melt is strongly fractionated relative to chondrites, indicating substantial high-temperature processing of the precursor materials in the solar nebula before parent body accretion (*17*, *18*). Relative to other refractory siderophile elements, W is depleted, reflecting either core formation under relatively oxidized conditions—where W becomes less siderophile—or subchondritic W abundances of the bulk IVB parent body with a bulk ^{180}Hf/^{184}W as high as ~2 (*9*). Using a ^{180}Hf/^{184}W of 2 results in a Hf-W model age of metal segregation of 1.8 ± 0.3 My after CAI formation, which is in good agreement with the timing of pure Fe metal melting inferred for the IIAB, IID, IIIAB, and IVA parent bodies (Fig. 4). The IVB parent body, therefore, may have accreted at about the same time as the other bodies.

The Hf-W results indicate that core formation in iron meteorite parent bodies occurred over at least ~1 My. Differences in the time of metal segregation reflect either distinct melting temperatures of the metal or variations in the proportions of early- and late-segregated metal fractions, which in turn are controlled by the bulk S concentrations of the parent bodies. Regardless of differences in the time of core formation, the parent bodies of the IIAB, IID, IIIAB, IVA, and IVB iron meteorites probably accreted at about the same time, between ~0.1 and ~0.3 My after CAI formation. Our data, therefore, rule out the possibility that strongly volatile-depleted parent bodies (IVA and IVB) accreted much earlier than less depleted bodies (IIAB), indicating that the variable depletions of moderately volatile elements in the iron meteorite parent bodies do not mirror the increasing condensation of the moderately volatile elements in the solar nebula over time. Rather, they seem to reflect more local processes within the nebula, resulting in spatially distinct chemical heterogeneities and thus variable volatile depletions of the dust accreting to planetesimals. This is consistent with the observation that the IVB iron meteorites, which are among the most strongly volatile-depleted meteorites, formed from material that underwent substantial high-temperature processing before parent body accretion.

REFERENCES AND NOTES

1. E. R. D. Scott, J. T. Wasson, *Rev. Geophys.* **13**, 527 (1975).
2. T. Kleine, K. Mezger, H. Palme, E. Scherer, C. Münker, *Geochim. Cosmochim. Acta* **69**, 5805–5818 (2005).
3. A. Scherstén, T. Elliott, C. Hawkesworth, S. Russell, J. Masarik, *Earth Planet. Sci. Lett.* **241**, 530–542 (2006).
4. A. Markowski, G. Quitte, A. Halliday, T. Kleine, *Earth Planet. Sci. Lett.* **242**, 1–15 (2006).
5. L. Qin, N. Dauphas, M. Wadhwa, J. Masarik, P. E. Janney, *Earth Planet. Sci. Lett.* **273**, 94–104 (2008).
6. T. Kleine *et al.*, *Geochim. Cosmochim. Acta* **73**, 5150–5188 (2009).
7. T. S. Kruijer *et al.*, *Earth Planet. Sci. Lett.* **361**, 162–172 (2013).
8. N. Wittig, M. Humayun, D. Brandon, S. Huang, I. Leya, *Earth Planet. Sci. Lett.* **361**, 152–161 (2013).
9. Materials and methods and supplementary text are available on *Science* Online.
10. T. S. Kruijer, T. Kleine, M. Fischer-Gödde, C. Burkhardt, R. Wieler, Hf-W isochron for bulk CAI: Evidence for homogeneity of ^{26}Al and ^{182}Hf. Paper presented at the 45th Lunar and Planetary Science Conference, Houston, TX, 17 to 21 March 2014, no. 1786.
11. T. Kleine, K. Mezger, C. Münker, H. Palme, A. Bischoff, *Geochim. Cosmochim. Acta* **68**, 2935–2946 (2004).
12. A. P. Boss, in *Origin of the Earth*, H. E. Newsom, J. Jones, Eds. (Oxford Univ. Press, Oxford, 1990), pp. 3–15.
13. M. Humayun, P. Cassen, in *Origin of the Earth and Moon*, R. Canup, K. Righter, Eds. (Univ. of Arizona Press, Tucson, AZ, 2000), pp. 3–23.
14. R. Brett, P. M. Bell, *Earth Planet. Sci. Lett.* **6**, 479–482 (1969).
15. Y. Fei, C. M. Bertka, L. W. Finger, *Science* **275**, 1621–1623 (1997).
16. T. Yoshino, M. J. Walter, T. Katsura, *Nature* **422**, 154–157 (2003).

17. A. J. Campbell, M. Humayun, *Geochim. Cosmochim. Acta* **69**, 4733–4744 (2005).
18. R. J. Walker *et al.*, *Geochim. Cosmochim. Acta* **72**, 2198–2216 (2008).
19. G. K. Benedix, H. Haack, T. J. McCoy, in *Treatise on Geochemistry* (Elsevier, Amsterdam, ed. 2, 2014), pp. 267–285.

ACKNOWLEDGMENTS

We thank T. Elliott, A. Halliday, and an anonymous reviewer for their comprehensive and constructive reviews. We gratefully acknowledge the Field Museum of Natural History (Chicago), the Smithsonian Institution (Washington, DC), and the American Museum of Natural History (New York City) for providing the samples for this study. We also thank R. Wieler, J. Wasson, R. Hin, F. Nimmo, and W. van Westrenen for discussions and U. Heitmann for technical support during sample preparation. This study was supported by a Förderungsprofessur to T.K. of the Swiss National Science Foundation (grant no. PP00P2_123470) and NASA Cosmochemistry grant NNX13AF83G to R.J.W.. The data reported in this paper are tabulated in the supplementary materials (tables S1 to S6).

SUPPLEMENTARY MATERIALS

www.sciencemag.org/content/344/6188/1150/suppl/DC1
Materials and Methods
Supplementary Text
Figs. S1 to S5
Tables S1 to S6
References (*20*–*39*)

4 February 2014; accepted 28 April 2014
10.1126/science.1251766

SENSORY BIOLOGY

Marine teleost locates live prey through pH sensing

John Caprio,[1]* Mami Shimohara,[2] Takayuki Marui,[3] Shuitsu Harada,[4] Sadao Kiyohara[2]

We report that the Japanese sea catfish *Plotosus japonicus* senses local pH-associated increases in H^+/CO_2 equating to a decrease of ≤0.1 pH unit in ambient seawater. We demonstrated that these sensors, located on the external body of the fish, detect undamaged cryptic respiring prey, such as polychaete worms. Sensitivity is maximal at the natural pH of seawater (pH 8.1 to 8.2) and decreases dramatically in seawater with a pH <8.0.

Locating food is essential for the survival of any heterotrophic organism. Sensory systems such as vision, hearing, and chemoreception aid in this critical endeavor, because each can provide key information for identifying and locating prey at a distance. Vision is of limited use for species that are nocturnal and/or live in murky environments (such as fish). Chemoreception, however, is especially important for many aquatic organisms in acquiring food (*1*).

While investigating how chemical stimulus information is encoded by the taste system in fish, we discovered a remarkable sensitivity of the Japanese sea catfish (*Plotosus japonicus*) to small transient increases in ambient H^+/CO_2. Extracellular electrophysiological recordings from specific fibers of the facial [cranial nerve VII)/cranial nerve V (trigeminal)] nerve complex that innervates the maxillary barbel (the "whisker") of the catfish (*2*) (Fig. 1A) were excited by slight transient declines in the pH of the ambient seawater (SW) that contacted its barbel (Fig. 1B). These fibers characteristically elicited large-amplitude (hundreds of microvolts to 1 mV) action potentials that were often about double the amplitude of those evoked by other fibers of the nerve complex recorded extracellularly. The recordings revealed that the fibers responded to a decline of ≤0.1 pH unit in SW that washed over the maxillary barbel (Fig. 1B and table S1) (*3*), a similar sensitivity to pH as that observed for respiratory chemosensitive neurons (*4*) and associated astrocytes (*5*) in the mammalian medulla. Not only did small-volume transients (fig. S1) (*3*) and repetitive (fig. S2) (*3*) declines in pH in the SW bathing the barbel receptive field (RF) activate the "pH fibers," the fibers also responded to larger transient drops, even those into the slightly acidic range (Fig. 1C). If the pH of the SW bathing the RF was lowered to <pH 8.0 and maintained for several minutes, either a greater drop in pH was required to activate the same fibers or the fibers became inactivated (table S1 and Figs. 1D, 2, and 3) (*3*). When the flow of control SW (pH ~8.2) over the RF was resumed, however, sensitivity to falling pH was restored (Figs. 1D and 4).

Because sea catfish are benthic nocturnal feeders (*6*) whose stomach contents contain polychaete worms (*7*), we hypothesized that a function of the highly sensitive H^+/CO_2 system of the catfish is to detect polychaete worms, which live in semipermanent U- or Y-shaped burrows in coastal marine sediments (*8*) and release punctate

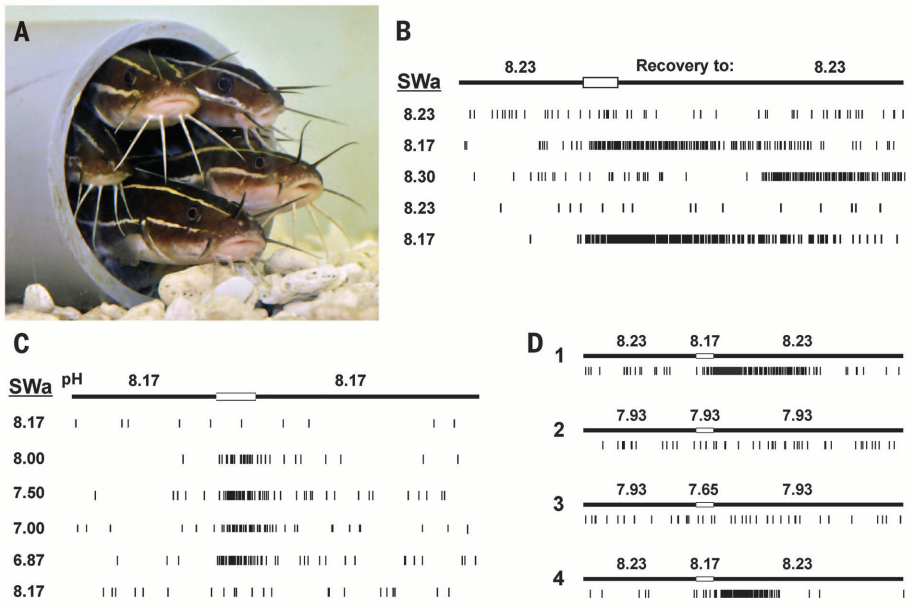

Fig. 1. Representative single nerve fibers that innervate the maxillary barbel respond to the falling pH of ambient SW. (**A**) Sea catfish, *Plotosus japonicus*. (**B**) Only falling pH activates the fiber. Artificial SW (SWa) of pH 8.23 flows over the barbel into which SW of either pH 8.23 (control), 8.17, or 8.3 is added (marked by the clear portion of the stimulus bar). Only falling pH activates the pH fiber (at stimulus onset for SW of pH 8.17 or with a delay after the onset of pH 8.30 SW) as the pH 8.23 SW background replaces the brief application of pH 8.30 SW. (**C**) A typical pH fiber is excited by brief applications of SW of pH < ambient, even to pH values into the acidic range. (**D**) SW of pH <8.0 that continuously bathes the barbel reduces the sensitivity of the sensor and sometimes inactivates the sensor (traces 2 and 3); however, sensitivity recovers to approximately control level (trace 4) after the barbel is bathed in pH 8.23 SW. The clear portion of the stimulus bar represents a 0.5-s stimulus presentation. Fibers shown in (B) to (D) are from different preparations.

[1]Department of Biological Sciences, Louisiana State University, Baton Rouge, LA 70803, USA. [2]Graduate School of Science and Engineering, Department of Chemistry and BioScience, Kagoshima University, Kagoshima 890-0065, Japan. [3]409 Koyocho, Sukagawa, Fukushima, 962-0401, Japan. [4]Department of Oral Physiology, Graduate School of Medical and Dental Sciences, Kagoshima University, Kagoshima 890-8544, Japan.
*Corresponding author. E-mail: jcap@lsu.edu